Mammary Tissue-Derived Extracellular Matrix Hydrogels Reveal the Role of the Irradiated Microenvironment in Breast Cancer Recurrence

Tian Zhu[1], Steven M. Alves[1], Ariana Adamo[2], Xiaona Wen[1], Kevin C. Corn[1], Anastasia Shostak[1], Nicholas D. Shaub[1], Benjamin C. Hacker[1], Antonio D'Amore[2], Rizia Bardhan[3,4], and Marjan Rafat[1,5,6,*]

[1]Department of Chemical and Biomolecular Engineering, Vanderbilt University, Nashville, TN, USA
[2]Department of Surgery, University of Pittsburgh, Pittsburgh, PA, USA
[3]Department of Chemical and Biological Engineering, Iowa State University, Ames, IA, USA
[4]Nanovaccine Institute, Iowa State University, Ames, IA, USA
[5]Department of Biomedical Engineering, Vanderbilt University, Nashville, TN, USA
[6]Department of Radiation Oncology, Vanderbilt University Medical Center, Nashville, TN, USA

*Author for correspondence: Marjan Rafat, Engineering and Science Building, Rm. 426, Vanderbilt University, Nashville, TN 37212. Phone: (615) 343-3389, Fax: (615) 343-7951, E-mail: marjan.rafat@vanderbilt.edu

Abstract

Radiation therapy (RT) is essential for triple negative breast cancer (TNBC) treatment. However, patients with TNBC continue to experience recurrence after RT. The alteration of extracellular matrix (ECM) of healthy breast tissue induced by radiation and its role on tumor recurrence are still unknown. In this study, we evaluated the structure, molecular composition, and mechanical properties of irradiated murine mammary fat pads (MFPs) and developed ECM hydrogels from decellularized tissues to assess the effects of RT-induced ECM changes on breast cancer cell behavior. Irradiated MFPs were characterized by increased ECM deposition and fiber density compared to unirradiated controls, which may provide a platform for cell invasion and proliferation. Alterations in irradiated ECM components including collagen I, IV, VI, and fibronectin were observed. TNBC cell proliferation was enhanced in irradiated hydrogels. Encapsulated TNBC cell morphology analysis indicated an increase in invasive capacity within irradiated ECM hydrogels. In addition, TNBC cells co-cultured with macrophages in irradiated ECM hydrogels exhibited further increases in cell proliferation. Our study establishes that the ECM in the irradiated microenvironment promotes TNBC invasion and proliferation that is enhanced in the presence of macrophages. This work represents an important step toward elucidating how changes in the ECM after RT contribute to breast cancer recurrence.

Keywords: Radiation therapy; Breast cancer recurrence; ECM hydrogels; Proliferation; Invasion; Macrophages

1. Introduction

Breast cancer is the second leading cause of cancer related mortality in women [1]. One widely used treatment for patients with breast cancer is radiation therapy (RT), which typically enhances antitumor effects and eliminates residual tumor cells after surgery and chemotherapy. However, approximately 20% of breast cancer patients suffer locoregional recurrence after initial treatment, especially in triple-negative breast cancer (TNBC) where patients have higher mortality compared to other subtypes [2,3]. Over 13% of treated TNBC patients suffer local recurrence at the primary site [4]. Previous work has shown that radiation can induce excess macrophage infiltration and ultimately tumor cell recruitment under immunocompromised conditions, suggesting that recurrence following RT may be dependent on immune status [5,6]. Therefore, understanding mechanism behind recurrence post-RT in TNBC is critical for improved patient survival.

Extracellular Matrix (ECM) in the tumor microenvironment plays a major role tumor progression and metastasis. ECM structure, composition, and mechanical properties have profound effects on cell and tissue phenotype. Recent studies have revealed that ECM deposition is altered by RT-induced fibrosis and tumor cells grow differently depending on the ECM tissue origin [7,8]. We are therefore motivated to determine the effect of the irradiated ECM on tumor and immune cell behavior, which has not yet been explored. A variety of synthetic hydrogels have been designed to study the impact of ECM on cell behavior; however, these synthetic systems have many limitations in recapitulating the native ECM. Decellularized ECM (dECM) hydrogels prepared from mammalian organs retain the composition of the original tissue and are considered promising biological scaffolds for cell cultivation and tissue regeneration. For example, dECM hydrogels have been engineered from multiple organs, including adipose tissue, dermis or urinary bladder, and then applied to cell culture *in vitro* or as natural injectable materials to repair and reconstruct tissues *in vivo* [9–11]. In this study, we developed decellularized ECM hydrogels to replicate the *in vivo* adipose tissue microenvironment and study the influence of the irradiated ECM on tumor recurrence *in vitro*.

We hypothesized that RT-induced ECM alterations may contribute to local recurrence by facilitating tumor cell growth and invasion. To test this hypothesis, we first analyzed the structure, composition, and mechanical properties of mammary fat pads (MFPs) following irradiation. We then fabricated dECM hydrogels from murine MFPs and evaluated the role of the irradiated ECM on tumor and immune cell behavior. This work represents a crucial step toward elucidating how modulation of the ECM after RT contributes to breast cancer recurrence.

2. Methods and Materials

2.1 Animals

Animal studies were performed in accordance with institutional guidelines and protocols approved by the Vanderbilt University Institutional Animal Care and Use Committee. 8-10 weeks-old female Nu/Nu mice were obtained from Charles River Laboratories. The mice were allowed free access to standard diet and water and maintained under a 12-hr light/12-hr dark cycle.

2.2 Preparation of MFP-derived ECM hydrogels

MFP-derived ECM was prepared as previously described [12]. In brief, MFPs were harvested from sacrificed nude mice using CO_2 asphyxiation followed by cervical dislocation and were then irradiated at a dose of 20 Gy *ex vivo* using a cesium source. After two days incubation in a 37°C/5% CO_2 incubator, MFPs were subsequently stored at -80°C overnight. Thawed MFPs were treated with 0.02% trypsin/0.05% EDTA (Gibco) for 1 hr, 2% Triton-X-100 (Sigma) for 1hr, 4% deoxycholic acid (Frontier Scientific) for 1hr, 1% penicillin-streptomycin (Gibco) at 4°C overnight, and 4% ethanol/0.1% peracetic acid (Sigma) for 2hr, followed by four 15 min washes of phosphate-buffered saline (PBS), n-propanol (Fisher Scientific) incubation for 1hr, and four 15 min washes of deionized water. Decellularized MFPs were then frozen and lyophilized for use in hydrogel preparation. The lyophilized MFPs ECM samples were ground into powder and mixed into 0.1 M hydrochloric acid–pepsin solution (1 mg/ml) (Sigma) at a ratio of 20 mg/ml, and enzymatically digested for 48hr under a constant stir rate at room temperature. The digestion was ended by titration to pH 7.4 with 1 M NaOH and a 10 × PBS (Quality Biological, Inc.) bringing the pre-gel solution to 1x PBS. The hydrogel is liquid at room temperature and solidifies at 37°C for 30 min.

2.3 Cell lines

GFP- and luciferase-labeled 4T1 mouse mammary carcinoma cells were obtained from Dr. Laura Bronsart (Stanford University). Unlabeled 4T1 cells were obtained from ATCC. MDA-MB-231 human breast cancer parental cells were obtained from Dr. Amato Giaccia (Stanford University). MDA-MB-231 cells were transduced with retrovirus particles encoding for the expression of firefly luciferase gene. All cells were cultured at 37°C and 5% CO_2. Bone marrow derived macrophages (BMDMs) were isolated from the femurs of 8-10 weeks-old female Nu/Nu mice. All cell lines tested negative for *Mycoplasma* contamination with the MycoAlert Mycoplasma detection kit (Lonza). 4T1 cells were cultured in in RPMI-1640 (Gibco), MDA-MB-231 were cultured in DMEM (Gibco), and both were supplemented with 10% fetal bovine serum (FBS) (Sigma) and antibiotics (100 U/mL penicillin and 100 mg/mL streptomycin) (Sigma). Isolated BMDMs were cultured in IMDM

(Gibco) supplemented with 10% fetal bovine serum (FBS) (Sigma), 10 ng/mL macrophage colony stimulating factor (MCSF), and antibiotics (100 U/mL penicillin and 100 mg/mL streptomycin) for 7d for maturation into macrophages.

2.4 Cell culture in ECM hydrogels

GFP- and luciferase-labeled 4T1 and unlabeled 4T1 were seeded in ECM hydrogels at a concentration of 100,000 or 500,000 cells/mL of pre-gel solution, respectively. Luciferase-labeled MDA-MB-231 were encapsulated in ECM hydrogels at a concentration of 500,000 or 1,000,000 cells/mL of pre-gel solution. 100uL of the gel-cell solution was added into each well of a 16-well chamber slide. Cells were thoroughly mixed in the pre-gel and then incubated at 37°C for 30 min. 100 μL of complete RPMI (Gibco) media for 4T1 or complete DMEM (Gibco) media for MDA-MB-231 was added to each well. After culturing at 37°C for 48hr, cell proliferation was measured by adding luciferin (0.167mg/mL) to the wells for 10 min and performing bioluminescence imaging (Caliper LifeSciences IVIS Lumina Series III). The GFP-labeled cells were also visualized using fluorescence microscopy at 0 hr, 24 hr, and 48 hr after gelation.

BMDMs were seeded in ECM hydrogels at concentrations of 500,000 or 1,000,000 cells/mL of pre-gel solution. 100uL of gel-cell solution was added into each well of a 16-well chamber slide. Cells were thoroughly mixed in the pre-gel and then incubated at 37°C for 30 min. 100 μL of complete IMDM (Gibco) media were added to each well, and cells were cultured at 37°C for 48hr. For co-culture experiments, BMDMs (1,000,000 cells/mL) were stained by CellTrace™ Far Red Cell Proliferation Kit (Thermo Fisher Scientific) in advance and cultured in 100μL pre-gel solution with GPF- and luciferase-labeled 4T1 (500,000 cells/mL). 50 μL of complete IMDM (Gibco) media, 50 μL of complete RPMI (Gibco) media and 0.1 μL MCSF were added to each well after gel formation and subsequently incubated at 37°C for 48 hr. Both cell lines were visualized using fluorescence microscopy at 0, 24, and 48 hours post-gelation. Proliferation of 4T1 cells were quantified by bioluminescence measurements at 48hr. Cell number per field of 4T1 cells and BMDM were analyzed using ImageJ (National Institutes of Health).

2.5 Live/Dead assay

The viability of cells was examined by the LIVE/DEAD™ Cell Viability Assay Kit (Molecular Probes, Inc.) 48hr after gelation. In brief, encapsulated unlabeled 4T1s or BMDMs were washed twice in Dulbecco's PBS (DPBS) (Gibco). 100 μL of DPBS containing 1 μM calcein AM (excitation/emission = 494/517 nm) and 2 μM ethidium homodimer (excitation/emission = 528/645

nm) were then added to the wells and measured using a Varioskan plate reader (ThermoFisher) after 30 min. Cells were then visualized by fluorescence microscopy (Leica DMi8).

2.6 Scanning electron microscopy (SEM) tissue preparation and quantification

MFP structure was examined using SEM, and the fiber network characteristics were quantified using a previously developed image analysis algorithm run on MATLAB software [13]. MFPs were fixed in cold 2% (v/v) glutaraldehyde with 4% paraformaldehyde in 0.1M Cacodylate Buffer for 4 hr followed by one wash in the same buffer. Fixed tissues were placed in 1% aqueous OsO_4 for 1hr and then washed by milli Q water twice. MFPs were dehydrated in a graded series of alcohol (50, 70, 90, 100% ethanol in deionized water) for 10 min per wash and then left in 100% ethanol overnight at 4 °C. After 3 additional 45 min changes in 100% ethanol, MFPs were slowly critical point dried. After drying, tissues were sputter coated with a 4.5 nm thick gold/palladium alloy coating and imaged with SEM. A complete set of fiber network descriptors was collected from SEM images of each MFPs: fiber alignment, node density (number of fiber intersections per mm^2), and fiber diameter. Fiber alignment was described through the normalized orientation index where 0% represents a randomly organized (isotropic) network while 100% represents a completely aligned (anisotropic) network. Porosity was described through the mean of the pore size histogram (mm^2). Automated extraction of these fiber architectural features was achieved with an algorithm, which has been previously described in detail [13]. Briefly, the SEM image is digitally processed by a cascade of steps, including equalization with a 3x3 median filter, local thresholding through the Otsu method, thinning, smoothing, morphological operators, skeletonization, binary filtering for Delaunay network refinement, and ultimately the detection of fiber network architecture and its descriptors.

2.7 Raman spectroscopy

MFPs were fixed by 10% neutral buffered formalin (NBF) for 24 hr at 4 °C and submerged in 30% sucrose for 48 hr at 4 °C. The fixed samples were then embedded in OCT and cut into 5 μm sections onto Raman grade CaF_2 disks. The Raman measurements were taken with 5s exposure time using a Renishaw inVia Raman microscope system with a 785 nm laser that delivered ~30 mW of power. A ×100 objective lens was used to focus a laser spot on the surface of samples.

2.8 Atomic force microscopy (AFM)

MFPs or ECM hydrogels were cut into 1mm x 1mm x 1mm pieces and each specimen was immobilized on 22mm x 22mm coverslip with a thin layer of two-component fast drying epoxy glue

(Devcon). All AFM indentations were performed using a Bruker inverted optical AFM and silicon nitride triangle cantilever with a 10-µm diameter borosilicate spherical tips (205-mm-long DNP-S10 triangular silicon nitride cantilevers, resonance frequency (air) f =18 kHz, nominal cantilever spring constant k = 0.08 Nm, tip radius = 5 µm, Bruker). The exact spring constant k of the cantilever was determined before each experiment using the thermal tune method and the deflection sensitivity was determined in fluid using glass substrates as an infinitely stiff reference material. Force-distance (FD) measurements of excised tissues were performed in a fluid cell. Samples were indented with a calibrated force of 5 nN and the Hertz model of impact was used to determine the elastic properties of the tissue.

2.9 Luminex multiplex immunoassay

Conditioned media (CM) from GPF- and luciferase-labeled 4T1 cultured in ECM hydrogels was collected after 2 days. Supernatant following centrifugation at 1100rpm to remove cells were stored at -80°C until processed. Three replicates were collected independently. All samples were evaluated using a mouse 32-plex Affymetrix kit (Eve Technologies Corporation).

2.10   Histological analysis and immunofluorescence

MFPs were removed from 8-10 week-old female Nu/Nu mice and irradiated to a dose of 20 Gy *ex vivo* using a cesium source. After 48hr incubation at 37°C in complete media, control and irradiated MFPs were fixed with 10% NBF for 48 hr, paraffin-embedded, and sectioned (5 µm). For hematoxylin and eosin (H&E) staining, standard procedures were followed for H&E, including deparaffinization, hydration, staining with hematoxylin (Sigma-Aldrich), and counterstaining with eosin (Sigma-Aldrich). For Masson's trichrome staining, including deparaffinization, rehydration, staining with Weigert's iron hematoxylin and Biebrich scarlet-acid fuchsin, differentiation in phosphomolybdic-phosphotungstic acid solution, and stained in aniline blue solution. For immunofluorescence staining, tissue sections (5 µm thick) were deparaffinized followed by antigen retrieval using 1X citrate buffer. After blocking in 10% goat serum, sections were incubated with primary antibodies, including anti-collagen I (1:200, Thermo Fisher Scientific), anti-collagen IV (1:200, Thermo Fisher Scientific), anti- collagen VI (1:200, Abcam) and anti-fibronectin (1:400, Thermo Fisher Scientific) overnight at 4°C. Fluorescently labeled secondary antibodies (Alexa Flour 488) were used to stain tissues for 1 hour at room temperature followed by applying Sudan Black B. Sections were mounted using ProLong glass antifade mountant with NucBlue stain (Thermo Fisher Scientific) and imaged using a fluorescence microscope. For F-actin staining, cells after 48 hr incubation were fixed in 10% NBF for 10 mins and washed with PBS. Cell

membranes were permeabilized by 0.1% Triton-100 in PBS for 5 min and washed by PBS. Cells were then incubated with phalloidin (Phalloidin-iFluor 594; Abcam) for 1 h at room temperature and washed by PBS. For cortactin staining, cells after fixation and permeabilization by similar methods were blocked with 5% NGS in PBS for 1hr at room temperature. Cells were incubated with anti-cortactin (1:50, Novus Biologicals) primary antibody in 1% BSA/PBS overnight at 4°C followed by three washes in PBS. Cells were then incubated with secondary antibodies (goat anti-rabbit IgG Alexa-Fluor 488; Thermo Fisher Scientific) for 1 hr at RT and washed with PBS. Chambers were removed and mounted on a glass slide with ProLong glass with NucBlue.

2.11 Patient data analysis

We used The Cancer Genome Atlas (TCGA) and Genotype-Tissue Expression (GTEx) tools to obtain patient mRNA expression. The TCGA TARGET GTEx study was accessed through the University of California Santa Cruz's Xena platform on May 3rd, 2022 to evaluate how gene expression of *Col4A3BP* and *Col4A2-S1* in the normal adjacent tissue of breast cancer patients correlated with patient outcome. The Xena visualization tool was used (https://xenabrowser.net/) to access the TCGA TARGET GTEx dataset, and a Kaplan Meier curve was generated. To investigate breast cancer patient gene expression, we accessed mRNA data from the TCGA cBioPortal (PanCancer dataset, n = 1,082 patients) on May 10th, 2022. From these data, the correlation of collagen, invadopodia, and secreted cytokines gene was determined. We also interrogated publicly available datasets though KMplotter (kmplot.com), which is a meta-analysis tool. TNBC patients were filtered based on ER, PR, and HER2 positivity. TNBC patients were used for analysis and stratified based on high or low expression of CCL2 with data were reported as probability of survival.

2.12 Statistical analysis

To determine statistical significance, BLI data were analyzed in a general linear model (ANOVA). Post hoc analyses were performed with a Tukey adjustment for multiple comparisons. In each experiment, obtained data are presented as the mean ± standard error of mean (SEM), difference among more than two groups was tested using the one-way analysis of variance (ANOVA), and that between two groups was evaluated by the independent sample Student's t test. $p < 0.05$ was considered significant. All analyses were performed using GraphPad Prism 9. A custom MATLAB code was used to perform smoothing and biological fluorescent background subtraction of Raman spectra. Smoothing of the data were done by following the Savitzsky and Golay method with fifth order and coefficient value of 33. A modified polynomial fit method was performed to subtract the

background fluorescence. A polynomial with seventh order was used to fit the Raman spectra with threshold of 0.0001.

3. Results

3.1 Structure and composition of control and irradiated MFPs

SEM images of the MFPs at different magnifications revealed more ECM fibers covering irradiated adipose cells as well as thinner and denser fibers (**Fig. 1A-D**). We subsequently quantified ECM fiber network characteristics using fiber network analysis software to confirm our qualitative observations [13] (**Fig.1E-H**). Collagen deposition was evaluated by the fiber covered area ratio parameter, which increased significantly after radiation (p<0.01) (**Fig. 1E**). Visual inspection of the algorithm output showed accurate automatic detection of the fiber network for control and irradiated MFPs (**Supplemental Fig. 1A**). Both fiber diameter and pore size decreased significantly in irradiated MFPs (p<0.05) (**Fig. 1F-G**). The node density of irradiated MFPs also increased significantly (**Fig. 1H**). However, the porosity and orientation index showed no significant changes between control and irradiated samples (**Supplemental Fig. 1B-C**).

We used Raman spectroscopy to evaluate the biochemical composition changes in the irradiated MFP (**Supplemental Fig. 2A**). The peaks at 1300 cm^{-1} are from lipids, which are responsible for vibrations of -(CH2)n- in-plane twist and fatty acids [14,15]. The peaks at 1265 cm^{-1} (amide III) and 1650 cm^{-1} (amide I) are from the collagen matrix [16,17]. **Supplemental Figs. 2B-C** show that both collagen/lipid ratio (Amide I / lipid and Amide III/ lipid) increased significantly in MFPs (p<0.01) after RT, confirming the increase in ECM deposition observed using SEM images. In an effort to elucidate the biochemical changes between irradiated and control samples, we used principal component analysis (PCA) [18]. PCA simplifies the complexity of high-dimensional data while retaining relevant information necessary for classification [19][20]. In a two-dimensional PC scatter plot, the first principal component (PC1) and the second principal component (PC2) showed a clear separation between the control and irradiated groups with a variance level of 29.36% for PC1 and 9.66% for PC2, again confirming compositional changes induced by RT (**Supplemental Fig. 2D**). Normalized Raman spectra peak analysis (**Table 1**) validate this difference, especially at the collagen peaks.

3.2 Mechanical properties and ECM component analysis

SEM images and Raman spectroscopy results indicated that ECM fibers increased in irradiated MFPs. To characterize the impact of increased ECM fibers on tissue biomechanical properties,

AFM was used to determine the stiffness of MFPs. FD measurements (**Supplementary Fig. 3**) were taken to determine Young's moduli [21]. The range of elastic moduli for control and irradiated breast tissue is shown in **Fig. 2A** and **Fig. 2B**. The histogram of stiffness values from control MFPs reveals a bimodal stiffness distribution with two prominent peaks at 0.2 ± 0.2 kPa ('peak 1') and 0.6 ± 0.2 kPa ('peak 2') (**Fig. 2A**). In comparison, irradiated MFPs exhibits a bimodal stiffness distribution with two prominent peaks at 0.4 ± 0.2 kPa ('peak 1'), 1 ± 0.2 kPa ('peak 2'). At values higher than 2 kPa, a broadening in the distribution indicates a marked mechanical heterogeneity across the sample. The average Young's modulus for irradiated MFPs was 2.4-fold greater than control MFPs (**Fig. 2B**). H&E staining confirmed an increase in overall ECM in irradiated MFPs (**Supplementary Fig. 4**). To determine how ECM components in normal breast tissue impact patient outcomes, we obtained mRNA expression data of patients with normal breast tissue from TCGA Target GTEx datasets. We found that high mRNA expression of *Col4A3BP* and *Col4A2-S1* were associated with poor overall survival (**Fig. 2C**). The link between collagen IV and poor outcomes in breast tissue led us to investigate the change of ECM components in irradiated breast tissue. Following immunofluorescence staining, we found that collagen I, collagen IV, collagen VI, and fibronectin (FN) were increased in irradiated murine breast tissue (**Fig. 2D**). These data show that RT modulates the expression of ECM subcomponents and leads to changes in ECM deposition and stiffness, which may impact tumor behavior and negatively impact patient survival in breast cancer.

3.3 Decellularized ECM hydrogels

Motivated by the RT-induced increased ECM deposition which may provide a platform for cell migration and invasion, we next utilized a decellularization technique to extract ECM, develop ECM hydrogels, and encapsulate cells to observe their behavior. We start from an immunodeficient model to replicate *in vivo* conditions relevant to recurrence [6]. Murine MFPs were decellularized by a series of mechanical, chemical, and enzymatic methods [12]. The final volume of decellularized MFPs was 10–20% of the original adipose tissue. H&E staining confirmed the removal of cell nuclei while preserving tissue structure following decellularization (**Fig. 3A**). We verified the retention of ECM using Masson's trichrome staining as well as lipid removal using perilipin staining (**Fig. 3A**). Masson's trichrome staining displayed that collagen was the main component of decellularized MFPs (**Fig. 3A**). Immunofluorescence staining showed that collagen I, IV, VI, and FN (**Supplemental Figure 5**) were present in decellularized MFPs. The above results indicate that most of the extracellular components were preserved while the cells and lipids were removed from decellularized MFPs.

To evaluate the properties of control and irradiated ECM hydrogels, SEM and AFM were performed. SEM was utilized to determine the architecture of ECM hydrogels (**Fig. 3B**). Automatic fiber quantification of SEM images showed the parameters of fiber dimeter, node density and pore size altered in irradiated ECM hydrogels (**Fig. 3C**), which parallels the changes observed in irradiated MFPs. Furthermore, AFM measurements showed that the stiffness of ECM hydrogels from irradiated samples was significantly higher than those for control ECM hydrogels. Together, these data proved the integrity of ECM after decellularization and that the changes in decellularized ECM hydrogels between control and irradiated samples are consistent with control and irradiated MFPs.

3.4 Proliferation and invasion of breast cancer cells in ECM hydrogels

The decellularized MFPs were lyophilized and digested by pepsin to from hydrogels (**Fig. 4A**). We encapsulated 4T1 murine TNBC cells in ECM hydrogels, and the Live/Dead viability assay showed that ECM hydrogels are not cytotoxic to 4T1 cells (**Supplemental Fig. 6A-B**). The ratio of live to dead cells was higher in the irradiated group, indicating 4T1 cells proliferated in the irradiated ECM hydrogels (**Supplemental Fig. 6C**). Additionally, immunofluorescence images and bioluminescence quantification were used to detect the proliferation of 4T1 cells in ECM hydrogels (**Fig. 4B**). 4T1 cell proliferation increased significantly in irradiated ECM hydrogels compared to unirradiated controls ($p < 0.05$) (**Fig. 4B**). MDA-MB-231 human TNBC cells also showed enhanced proliferation in the irradiated microenvironment (**Supplemental Figure 7A-C**), suggesting that irradiated ECM hydrogels promote tumor cell proliferation.

We further visualized the cytoskeletal properties of 4T1 cells embedded in the ECM hydrogels. The driving force for cancer invasion into their surrounding microenvironment as well as numerous cellular physical processes is through localized actin filaments [22–25]. Therefore, we stained for F-actin using phalloidin, and cellular morphology was quantified in the irradiated ECM hydrogels (**Fig. 4C-D**). Cells in the irradiated group increased their elongation index ($p<0.05$) and reduced their form factor significantly ($p<0.05$) in the irradiated hydrogels, suggesting cell invasiveness is promoted in the irradiated microenvironment (**Fig. 4C-D**). We also examined invadopodia, which are protrusive structures that can remodel the ECM and facilitate invasive migration [26–28]. The colocalization of F-actin and cortactin are considered reliable indicators for invadopodia [29]. F-actin and cortactin colocalization revealed significantly more invadopodia in 4T1 cells within the irradiated hydrogels ($p<0.05$), indicating a higher invasive capacity of 4T1 cells influenced by RT

(**Fig. 4C-D**). Tyrosine kinase substrate 4 (TKS4) and WASP interacting protein (WIP), which facilitate the activation of Neural Wiskott-Aldrich syndrome protein (N-WASP), are key molecular components that modulate invadopodia extension [30]. Clinical data from TCGA showed an association between the gene expression of collagen subtypes and TKS4 (*SH3PXD2B*) or WIP (*WIPF*) (**Supplemental Figure 8A-B**), indicating high invadopodia formation may be the result of increased microenvironmental collagen expression.

3.5 Co-culture of 4T1 and BMDM in ECM hydrogels

We collected CM from 4T1 cells encapsulated in the ECM hydrogels and analyzed cytokine secretion using a Luminex multiplex immunoassay. Factors with a 1.5-fold or greater increase in mean fluorescence intensity (MFI) are shown (**Fig. 5A**). To understand the relationship between ECM components, invadopodia, and cytokine secretion in a broader clinical context, TCGA analysis revealed a correlation between *Col4A4* and *CCL2* (MCP-1) gene expression (**Fig. 5B**). We also found a correlation between *Col4A4* and *IL6* mRNA expression (Fig. 5C), indicating the increased collagen IV levels in breast tissue after RT may elevate the secretion of cytokines in tumor cells. Further analysis of the TCGA PanCancer dataset showed *WIPF1* was associated with *CCL2* mRNA expression (**Fig. 5D**). This mirrors our finding that tumor cytokine secretion was enhanced in response to the increase in collagen IV after RT, and this facilitated increased invasion via invadopodia expression. These correlations serve to validate our Luminex data showing increased tumor cell secretion of CCL2 and IL6 in irradiated ECM hydrogels. To investigate the link between the CCL2 secretion and patient outcomes in TNBC, we utilized publicly available datasets through KMplotter. Among TNBC patients, high CCL2 expression was associated with poor patient survival (**Fig. 5E**). These data indicate that the increase in tissue collagen IV due to RT may lead to elevated levels of CCL2 in recruited tumor cells which in turn decrease patient survival. CCL2 expression is associated with macrophage infiltration and poor prognosis [31]. In addition, granulocyte macrophage colony-stimulating factor (GM-CSF) secreted from tumor cells in irradiated ECM hydrogels had the largest fold change compared to cells in unirradiated hydrogels, reaching nearly a 16-fold increase. Previous work has shown that increased GM-CSF levels after RT may lead to macrophage infiltration and attract circulating tumor cells [5,6]. We therefore evaluated how immune cells behave in the irradiated ECM hydrogels and how they interact with tumor cells. We isolated BMDMs from Nu/Nu mouse femurs and seeded them in ECM hydrogels. Live/Dead viability assay images and quantification showed increased BMDMs in the irradiated microenvironment (**Fig. 5F-H**). We then co-cultured the GFP-labeled 4T1 cells and BMDMs stained with CellTrace Far Red to evaluate the interactions

between tumor and immune cells in irradiated ECM hydrogels. Fluorescence images and bioluminescence measurements demonstrated an increase in 4T1 cells proliferation in the irradiated hydrogels. It is noteworthy that 4T1 cells co-cultured with BMDMs exhibited enhanced proliferation by 3-fold compared with proliferation of 4T1 cells cultured alone, suggesting that macrophages further promote tumor cell proliferation (**Fig. 5I-L**). BMDMs were also found to increase proliferation in the irradiated microenvironment when co-cultured with 4T1 cells (**Fig. 5M**).

4. Discussion

The poor overall survival in TNBC patients is associated with high incidence of local recurrence following RT, and previous work suggests a link between radiation damage and TNBC recurrence in immunocompromised mouse models [6]. Understanding how irradiation modulates the microenvironment is necessary for evaluating tumor recurrence mechanisms. We first analyzed the structural and compositional alterations of irradiated breast tissue and showed enhanced ECM deposition and stiffness following irradiation. As physicochemical cues dictated by changes in ECM deposition modulate numerous biological functions, we developed decellularized ECM hydrogels as models of the irradiated microenvironment to determine the impact of RT-induced ECM changes on tumor cell behavior. Increased ECM deposition and alterations in ECM components induced by RT enhance the stiffness of breast tissue, and we determined that this may lead to a favorable environment for TNBC recurrence by influencing both tumor and immune cells. Our study is the first to recapitulate the irradiated ECM microenvironment, and this model can be used as a platform for studying radiation response and recurrence mechanisms.

Following ionizing radiation, immune cells infiltrating injured sites lead to the recruitment and differentiation of fibroblasts, resulting in excess ECM deposition and fibrosis [7,33–35]. Furthermore, diseased ECM is usually denser and mechanically stiffer than normal ECM due to increased ECM deposition as well as structural changes in molecular composition such as the collagen content [36]. These findings are consistent with our SEM results showing excess ECM deposition and denser and thinner ECM fibers in irradiated samples. In addition, ECM quantity, density, and composition generally determine the stiffness and mechanical properties of breast tissue and significantly impact malignant cell invasion, survival, and proliferation [37,38]. AFM studies indicated that the stiffness of irradiated tissue increased due to the altered ECM. The stiffness range of human breast tissue is approximately 0.5-1 kPa [39], which is in the range of our findings.

Approximately 300 proteins present in the ECM have been reported to mediate cellular behaviors and tissue development, and collagen is the major abundant fibrous protein which constitutes up to 90% of the ECM [40]. 28 types of collagen have been described [41], and collagen I, IV and VI are the most relevant subtypes of collagens in the microenvironment of mammary tissue. A major function of collagen I, IV and VI in the local ECM environment is to provide structural support for cells and enrich the cell surface with growth factors and cytokines that are important in tumor progression. Increased collagen IV after chemotherapy has been shown to drive TNBC cell invasion [42]. Collagen VI is secreted by adipocytes and is known to regulate breast tumor development and facilitate TNBC cell migration [43,44]. In addition to collagens, other prominent fibrous proteins including elastins, fibronectins, and laminins also are related to cellular dynamics [45]. Enhanced fibronectins are crucial for attaching cells to matrix and guiding cell migration and have been reported in the RT-induced fibrosis process [46]. This agrees with our results showing that fibronectin quantity increased in irradiated MFPs. We also showed that changes in collagen deposition may provide more tensile strength and support tumor cell retention and invasion through direct cell-protein contact.

Variations in ECM density, composition, and stiffness have been correlated with tumor progression and recurrence [45]. To investigate the influence of altered ECM induced by RT on tumor and immune cell behavior, we developed an irradiated ECM hydrogel model to recapitulate *in vivo* conditions. Numerous polymer hydrogels like collagen hydrogels and Matrigel have been widely used to study cell behavior, but they have limitations due to the absence of native tissue structure or site-specific bioactive molecules such as exogenous growth factors or peptides [47,48]. The advantage of component integrity and robust biologic activity from constituent matrix molecules makes decellularized ECM hydrogels a promising method to mimic the irradiated microenvironment [49]. Our results confirm the preservation of ECM components. ECM hydrogels have been previously fabricated from various tissue sources like adipose tissue [10,50], liver [51], lung [52], dermis and urinary bladder [9] through different processing methods. The mechanical properties of ECM hydrogels have previously been characterized from 0.1kPa to 40kPa [9,53], which is consistent with our results. The differences in mechanical properties between normal and irradiated ECM hydrogels are likely due to variations in ECM structure and composition. Dermal-ECM hydrogels have a higher fiber node density than urinary bladder ECM hydrogels and a higher storage modulus, indicating a link between fiber node density and mechanical strength [54]. Additionally, the pore size, fiber density, and orientation in tissue derived ECM hydrogels, collagen I hydrogels, and Matrigel also lead to variations in mechanical

properties [55,56]. Our SEM images and fiber analysis showed that ECM fibers in irradiated ECM hydrogels were denser and correlated to stiffer hydrogels. Cell behavior is significantly modulated by the mechanical properties of their surrounding microenvironment. We showed that the varied ECM hydrogel structure and mechanical properties had a profound effect on cell invasion, survival, and proliferation.

Mammary tissue-derived ECM hydrogels were used to observe cell behavior in response to RT-induced ECM alterations. Tumor cell growth has been shown to be influenced by tissue-specific ECM [57], implicating that highly dynamic ECM plays an important role in tumor migration and metastasis. ECM not only provides a platform for cell migration but also has the ability to interact with cells directly through engagement with integrins [58]. Our results showed that proliferation of TNBC cells was increased in irradiated ECM hydrogels, which builds on previous findings linking the recruitment of tumor cells to irradiated sites to recurrence under immunocompromised conditions [6]. In addition, the tumor cells had a higher invasive capacity in the irradiated microenvironment. Together, we determined that the proliferation and invasion of breast cancer cells was enhanced through interacting with irradiated ECM.

Immune cells are recruited to RT-damaged sites by inflammatory mediators and secreted profibrotic cytokines such as TNF, IL-13, and TGF-β during fibrosis [7]. Furthermore, macrophages infiltrate irradiated normal tissue [59], and the presence of inflammatory macrophages has been correlated to recurrence and poor overall survival in breast cancer patients [60]. We did not model macrophage recruitment but instead showed that the irradiated microenvironment promotes macrophage infiltration through tumor secreted factors. Although increases in tumor cell proliferation also occur without macrophages in irradiated ECM hydrogels, the extent of cancer cell proliferation is greater during co-culture with macrophages. This suggests that the irradiated ECM influences tumor-immune cell interactions and may promote a pro-recurrent niche. This agrees with previous *in vivo* findings [5,6,32] showing that excess macrophage infiltration attracts circulating tumor cells and indicates that cross-talk with immune cells plays a pivotal role in tumor cell survival in irradiated tissues.

Overall, we developed a mammary-derived ECM hydrogel to model radiation response, which will lead to the discovery of novel targets for reducing TNBC recurrence and increasing breast cancer patient survival following therapy. We aimed to replicate *in vivo* conditions using ECM hydrogels to study the influence of the irradiated breast tissue on TNBC recurrence. We irradiated MFPs *ex

vivo, which may have different outcomes compared to *in vivo* radiation where cell infiltration may alter ECM remodeling. However, this model is valuable for analyzing the direct effect of radiation on changes in the ECM in the mammary gland. Future studies will evaluate the impact of *in vivo* RT on ECM-linked TNBC recurrence.

5. Conclusions

We demonstrate that decellularized ECM hydrogels are a useful tool to study the radiation response. ECM changes, including increased fiber deposition and stiffness, induced by radiation facilitate tumor cell proliferation and invasion. In addition, we showed that macrophages enhance TNBC cell proliferation in the irradiated microenvironment, which may drive TNBC recurrence following therapy.

Declaration of Competing Interests

The authors declare no known competing financial interests or personal relationships that could have appeared to influence the work reported in this paper.

Acknowledgments

References

[1]   Breast cancer facts & figures 2019–2020, Am. Cancer Soc. (2020) 1–44.

[2]   N.L. Simone, T. Dan, J. Shih, S.L. Smith, L. Sciuto, E. Lita, M.E. Lippman, E. Glatstein, S.M. Swain, D.N. Danforth, K. Camphausen, Twenty-five year results of the national cancer institute randomized breast conservation trial, Breast Cancer Res. Treat. 132 (2012) 197–203. https://doi.org/10.1007/s10549-011-1867-6.

[3]   B.G. Haffty, Long-term results of hypofractionated radiation therapy for breast cancer, Breast Dis. 21 (2010) 267–268. https://doi.org/10.1016/S1043-321X(10)79594-1.

[4]   A.J. Lowery, M.R. Kell, R.W. Glynn, M.J. Kerin, K.J. Sweeney, Locoregional recurrence after breast cancer surgery: a systematic review by receptor phenotype, Breast Cancer Res. Treat. 133 (2012) 831–841. https://doi.org/10.1007/s10549-011-1891-6.

[5]   M. Vilalta, M. Rafat, A.J. Giaccia, E.E. Graves, Recruitment of Circulating Breast Cancer Cells Is Stimulated by Radiotherapy, Cell Rep. 8 (2014) 402–409. https://doi.org/10.1016/j.celrep.2014.06.011.

[6]   M. Rafat, T.A. Aguilera, M. Vilalta, L.L. Bronsart, L.A. Soto, R. Von Eyben, M.A. Golla, Y. Ahrari, S. Melemenidis, A. Afghahi, M.J. Jenkins, A.W. Kurian, K.C. Horst, A.J. Giaccia, E.E. Graves, Macrophages promote circulating tumor cell-mediated local recurrence following radiotherapy in immunosuppressed patients, Cancer Res. (2018). https://doi.org/10.1158/0008-5472.CAN-17-3623.

[7]   H. Jin, Y. Yoo, Y. Kim, Y. Kim, J. Cho, Y.S. Lee, Radiation-induced lung fibrosis: Preclinical animal models and therapeutic strategies, Cancers (Basel). 12 (2020) 1–24. https://doi.org/10.3390/cancers12061561.

[8]   M. Blatchley, J.S. Bader, A. Pandey, D. Pardoll, Tissue matrix arrays for high throughput screening and systems analysis of cell function, 12 (2016) 1197–1204. https://doi.org/https://www.nature.com/articles/nmeth.3619.

[9]   M.T. Wolf, K.A. Daly, E.P. Brennan-Pierce, S.A. Johnson, C.A. Carruthers, A. D'Amore, S.P. Nagarkar, S.S. Velankar, S.F. Badylak, A hydrogel derived from decellularized dermal extracellular matrix, Biomaterials. 33 (2012) 7028–7038. https://doi.org/10.1016/j.biomaterials.2012.06.051.

[10]   L.E. Flynn, The use of decellularized adipose tissue to provide an inductive microenvironment for the adipogenic differentiation of human adipose-derived stem cells, Biomaterials. 31 (2010) 4715–4724. https://doi.org/10.1016/j.biomaterials.2010.02.046.

[11]   M.T. Spang, K.L. Christman, Extracellular matrix hydrogel therapies: In vivo applications and development, Acta Biomater. 68 (2018) 1–14. https://doi.org/10.1016/j.actbio.2017.12.019.

[12]   S.M. Alves, T. Zhu, A. Shostak, N.S. Rossen, M. Rafat, Studying normal tissue radiation effects using extracellular matrix hydrogels, J. Vis. Exp. (2019). https://doi.org/10.3791/59304.

[13]   A. D'Amore, J.A. Stella, W.R. Wagner, M.S. Sacks, Characterization of the complete fiber network topology of planar fibrous tissues and scaffolds, Biomaterials. 31 (2010) 5345–5354. https://doi.org/10.1016/j.biomaterials.2010.03.052.

[14]   J. Depciuch, E. Kaznowska, I. Zawlik, R. Wojnarowska, M. Cholewa, P. Heraud, J. Cebulski, Application of Raman Spectroscopy and Infrared Spectroscopy in the Identification of Breast Cancer, Appl. Spectrosc. 70 (2016) 251–263.

https://doi.org/10.1177/0003702815620127.

[15] Z. Movasaghi, S. Rehman, I.U. Rehman, Raman spectroscopy of biological tissues, Appl. Spectrosc. Rev. 42 (2007) 493–541. https://doi.org/10.1080/05704920701551530.

[16] R. Ahmed, A.W.L. Law, T.W. Cheung, C. Lau, Raman spectroscopy of bone composition during healing of subcritical calvarial defects, Biomed. Opt. Express. 9 (2018) 1704. https://doi.org/10.1364/boe.9.001704.

[17] Y. Ling, H.F. Rios, E.R. Myers, Y. Lu, J.Q. Feng, A.L. Boskey, DMP1 depletion decreases bone mineralization in vivo: An FTIR imaging analysis, J. Bone Miner. Res. 20 (2005) 2169–2177. https://doi.org/10.1359/JBMR.050815.

[18] S.K. Paidi, A. Rizwan, C. Zheng, M. Cheng, K. Glunde, I. Barman, Label-free raman spectroscopy detects stromal adaptations in premetastatic lungs primed by breast cancer, Cancer Res. (2017). https://doi.org/10.1158/0008-5472.CAN-16-1862.

[19] J. Lever, M. Krzywinski, N. Altman, Points of Significance: Principal component analysis, Nat. Methods. 14 (2017) 641–642. https://doi.org/10.1038/nmeth.4346.

[20] X. Wen, Y.C. Ou, G. Bogatcheva, G. Thomas, A. Mahadevan-Jansen, B. Singh, E.C. Lin, R. Bardhan, Probing metabolic alterations in breast cancer in response to molecular inhibitors with Raman spectroscopy and validated with mass spectrometry, Chem. Sci. 11 (2020) 9863–9874. https://doi.org/10.1039/d0sc02221g.

[21] F.M. Lartey, M. Rafat, M. Negahdar, A. V. Malkovskiy, X. Dong, X. Sun, M. Li, T. Doyle, J. Rajadas, E.E. Graves, B.W. Loo, P.G. Maxim, Dynamic CT imaging of volumetric changes in pulmonary nodules correlates with physical measurements of stiffness, Radiother. Oncol. 122 (2017) 313–318. https://doi.org/10.1016/j.radonc.2016.11.019.

[22] R. Zhao, A. Afthinos, T. Zhu, P. Mistriotis, Y. Li, S.A. Serra, Y. Zhang, C.L. Yankaskas, S. He, M.A. Valverde, S.X. Sun, K. Konstantopoulos, Cell sensing and decision-making in confinement: The role of TRPM7 in a tug of war between hydraulic pressure and cross-sectional area, Sci. Adv. 5 (2019). https://doi.org/10.1126/sciadv.aaw7243.

[23] J. Stricker, T. Falzone, M.L. Gardel, Mechanics of the F-actin cytoskeleton, J. Biomech. (2010). https://doi.org/10.1016/j.jbiomech.2009.09.003.

[24] P.A. Janmey, C.A. McCulloch, Cell mechanics: Integrating cell responses to mechanical stimuli, Annu. Rev. Biomed. Eng. 9 (2007) 1–34. https://doi.org/10.1146/annurev.bioeng.9.060906.151927.

[25] B. Emon, J. Bauer, Y. Jain, B. Jung, T. Saif, Biophysics of Tumor Microenvironment and Cancer Metastasis - A Mini Review, Comput. Struct. Biotechnol. J. 16 (2018) 279–287. https://doi.org/10.1016/j.csbj.2018.07.003.

[26] H. Paz, N. Pathak, J. Yang, Invading one step at a time: The role of invadopodia in tumor metastasis, Oncogene. 33 (2014) 4193–4202. https://doi.org/10.1038/onc.2013.393.

[27] G. Bati, D. Pesen Okvur, Invadopodia: Proteolytic feet of cancer cells, Turkish J. Biol. 38 (2014) 740–747. https://doi.org/10.3906/biy-1404-110.

[28] M.J. Breiding, Matrix Rigidity Differentially Regulates Invadopodia Activity Through ROCK1 and ROCK2, Physiol. Behav. 63 (2014) 1–18. https://doi.org/10.1016/j.biomaterials.2016.01.028.Matrix.

[29] M. Noi, K.I. Mukaisho, S. Yoshida, S. Murakami, S. Koshinuma, T. Adachi, Y. Machida, M. Yamori, T. Nakayama, G. Yamamoto, H. Sugihara, ERK phosphorylation functions in invadopodia formation in tongue cancer cells in a novel silicate fibre-based 3D cell culture system, Int. J. Oral Sci. 10 (2018) 1–10. https://doi.org/10.1038/s41368-018-0033-y.

[30] H. Yamaguchi, M. Lorenz, S. Kempiak, C. Sarmiento, S. Coniglio, M. Symons, J. Segall, R. Eddy, H. Miki, T. Takenawa, J. Condeelis, Molecular mechanisms of invadopodium formation: The role of the N-WASP-Arp2/3 complex pathway and cofilin, J. Cell Biol. 168 (2005) 441–452. https://doi.org/10.1083/jcb.200407076.

[31] X. Sun, D.J. Glynn, L.J. Hodson, C. Huo, K. Britt, E.W. Thompson, L. Woolford, A. Evdokiou, J.W. Pollard, S.A. Robertson, W. V. Ingman, CCL2-driven inflammation increases mammary gland stromal density and cancer susceptibility in a transgenic mouse model, Breast Cancer Res. 19 (2017) 1–15. https://doi.org/10.1186/s13058-016-0796-z.

[32] D.G. DeNardo, D.J. Brennan, E. Rexhepaj, B. Ruffell, S.L. Shiao, S.F. Madden, W.M. Gallagher, N. Wadhwani, S.D. Keil, S.A. Junaid, H.S. Rugo, E. Shelley Hwang, K. Jirström, B.L. West, L.M. Coussens, Leukocyte complexity predicts breast cancer survival and functionally regulates response to chemotherapy, Cancer Discov. 1 (2011) 54–67. https://doi.org/10.1158/2159-8274.CD-10-0028.

[33] K.M. Arnold, N.J. Flynn, A. Raben, L. Romak, Y. Yu, A.P. Dicker, F. Mourtada, J. Sims-Mourtada, The Impact of Radiation on the Tumor Microenvironment: Effect of Dose and Fractionation Schedules, Cancer Growth Metastasis. 11 (2018) 117906441876163. https://doi.org/10.1177/1179064418761639.

[34] J.M. Straub, J. New, C.D. Hamilton, C. Lominska, S.M. Thomas, Radiation-induced fibrosis: mechanisms and implications for therapy, Radiation-Induced Fibros. Mech. Implic. Ther. 141 (2016) 1–16. https://doi.org/10.1007/s00432-015-1974-6.Radiation-induced.

[35] T.J. Bledsoe, S.K. Nath, R.H. Decker, R a d i a t i o n Pn e u m o n i t i s Radiation pneumonitis Radiation complications Radiation fibrosis, 38 (2017) 6511.

[36] M.J. Breiding, Tumor-associated fibrosis as a regulator of tumor immunity and response to immunotherapy, Physiol. Behav. 63 (2014) 1–18. https://doi.org/10.1007/s00262-017-2003-1.Tumor-associated.

[37] V. Poltavets, M. Kochetkova, S.M. Pitson, M.S. Samuel, The role of the extracellular matrix and its molecular and cellular regulators in cancer cell plasticity, Front. Oncol. 8 (2018) 1–19. https://doi.org/10.3389/fonc.2018.00431.

[38] P. Lu, V.M. Weaver, Z. Werb, The extracellular matrix: A dynamic niche in cancer progression, J. Cell Biol. 196 (2012) 395–406. https://doi.org/10.1083/jcb.201102147.

[39] M.R. LOGAN A. NORTHCUTT1, ALEJANDRA SUAREZ-ARNEDO2, Emerging Biomimetic Materials for Studying Tumor and Immune Cell Behavior, Physiol. Behav. 63 (2014) 1–18. https://doi.org/10.1007/s10439-019-02384-0.Emerging.

[40] L.D. Muiznieks, F.W. Keeley, Molecular assembly and mechanical properties of the extracellular matrix: A fibrous protein perspective, Biochim. Biophys. Acta - Mol. Basis Dis. 1832 (2013) 866–875. https://doi.org/10.1016/j.bbadis.2012.11.022.

[41] B. Yue, Biology of the extracellular matrix: an overview, Bone. 23 (2012) 1–7. https://doi.org/10.1097/IJG.0000000000000108.Biology.

[42] J.P. Fatheree, J.R. Guarin, R.A. Mcginn, S.P. Naber, M.J. Oudin, A. Chemotherapy - induced collagen IV drives cancer cell motility through activation of Src and focal adhesion kinase, Cancer Res. 82 (2022). https://doi.org/10.1158/0008-5472.CAN-21-1823

[43] P. Iyengar, V. Espina, T.W. Williams, Y. Lin, D. Berry, L.A. Jelicks, H. Lee, K. Temple, R. Graves, J. Pollard, N. Chopra, R.G. Russell, R. Sasisekharan, B.J. Trock, M. Lippman,

V.S. Calvert, E.F. Petricoin, L. Liotta, E. Dadachova, R.G. Pestell, M.P. Lisanti, P. Bonaldo, P.E. Scherer, Adipocyte-derived collagen VI affects early mammary tumor progression in vivo, demonstrating a critical interaction in the tumor/stroma microenvironment, J. Clin. Invest. 115 (2005) 1163–1176. https://doi.org/10.1172/JCI23424.

[44] A.L. Wishart, S.J. Conner, J.R. Guarin, J.P. Fatherree, Y. Peng, R.A. McGinn, R. Crews, S.P. Naber, M. Hunter, A.S. Greenberg, M.J. Oudin, Decellularized extracellular matrix scaffolds identify full-length collagen VI as a driver of breast cancer cell invasion in obesity and metastasis, Sci. Adv. 6 (2020). https://doi.org/10.1126/sciadv.abc3175.

[45] D.M. Gilkes, G.L. Semenza, D. Wirtz, Hypoxia and the extracellular matrix: Drivers of tumour metastasis, Nat. Rev. Cancer. 14 (2014) 430–439. https://doi.org/10.1038/nrc3726.

[46] M. Ansems, P.N. Span, The tumor microenvironment and radiotherapy response; a central role for cancer-associated fibroblasts, Clin. Transl. Radiat. Oncol. 22 (2020) 90–97. https://doi.org/10.1016/j.ctro.2020.04.001.

[47] R.A. Stile, K.E. Healy, Thermo-responsive peptide-modified hydrogels for tissue regeneration, Biomacromolecules. 2 (2001) 185–194. https://doi.org/10.1021/bm0000945.

[48] M.W. Tibbitt, K.S. Anseth, Hydrogels as extracellular matrix mimics for 3D cell culture, Biotechnol. Bioeng. 103 (2009) 655–663. https://doi.org/10.1002/bit.22361.

[49] C. Matthew T. Wolfa, b, Kerry A. Dalyb, c, Janet E. Reingb, and Stephen F. Badylaka, b, c, Physiol. Behav. 63 (2014) 1–18. https://doi.org/10.1016/j.biomaterials.2011.12.055.Biologic.

[50] D.A. Young, D.O. Ibrahim, D. Hu, K.L. Christman, Injectable hydrogel scaffold from decellularized human lipoaspirate, Acta Biomater. 7 (2011) 1040–1049. https://doi.org/10.1016/j.actbio.2010.09.035.

[51] T.L. Sellaro, D. Ph, A. Ranade, D. Ph, D.M. Faulk, G.P. Mccabe, D. Ph, K. Dorko, S.F. Badylak, D. Ph, S.C. Strom, D. Ph, Maintenance of Human Hepatocyte Function In Vitro by Liver-Derived Extracellular Matrix Gels, Tissue Eng. Part A. 16 (2010).

[52] J. Zhou, P. Wu, H. Sun, H. Zhou, Y. Zhang, Z. Xiao, Lung tissue extracellular matrix-derived hydrogels protect against radiation-induced lung injury by suppressing epithelial–mesenchymal transition, J. Cell. Physiol. 235 (2020) 2377–2388. https://doi.org/10.1002/jcp.29143.

[53] R.H.J. De Hilster, P.K. Sharma, M.R. Jonker, E.S. White, E.A. Gercama, M. Roobeek, W. Timens, M.C. Harmsen, M.N. Hylkema, J.K. Burgess, Human lung extracellular matrix hydrogels resemble the stiffness and viscoelasticity of native lung tissue, Am. J. Physiol. - Lung Cell. Mol. Physiol. 318 (2020) L698–L704. https://doi.org/10.1152/AJPLUNG.00451.2019.

[54] P.L. Chandran, V.H. Barocas, Deterministic material-based averaging theory model of collagen gel micromechanics, J. Biomech. Eng. 129 (2007) 137–147. https://doi.org/10.1115/1.2472369.

[55] K.F. Ruud, W.C. Hiscox, I. Yu, R.K. Chen, W. Li, Distinct phenotypes of cancer cells on tissue matrix gel, Breast Cancer Res. 22 (2020) 1–22. https://doi.org/10.1186/s13058-020-01321-7.

[56] L. Cassereau, Y.A. Miroshnikova, G. Ou, J. Lakins, V.M. Weaver, A 3D tension bioreactor platform to study the interplay between ECM stiffness and tumor phenotype, J.

Biotechnol. 193 (2015) 66–69. https://doi.org/10.1016/j.jbiotec.2014.11.008.

[57]   V.Z. Beachley, M.T. Wolf, K. Sadtler, S.S. Manda, H. Jacobs, M.R. Blatchley, J.S. Bader, A. Pandey, D. Pardoll, J.H. Elisseeff, Tissue matrix arrays for high-throughput screening and systems analysis of cell function, Nat. Methods. (2015). https://doi.org/10.1038/nmeth.3619.

[58]   N. Cordes, Integrin-mediated cell-matrix interactions for prosurvivaland antiapoptotic signaling after genotoxic injury, Cancer Lett. 242 (2006) 11–19. https://doi.org/10.1016/j.canlet.2005.12.004.

[59]   J.W. Denham, M. Hauer-Jensen, The radiotherapeutic injury - A complex "wound," Radiother. Oncol. 63 (2002) 129–145. https://doi.org/10.1016/S0167-8140(02)00060-9.

[60]   C. Medrek, F. Pontén, K. Jirström, K. Leandersson, The presence of tumor associated macrophages in tumor stroma as a prognostic marker for breast cancer patients, BMC Cancer. 12 (2012) 1. https://doi.org/10.1186/1471-2407-12-306.

Tables

Table 1. Normalized representative peaks detected by Raman Spectroscopy

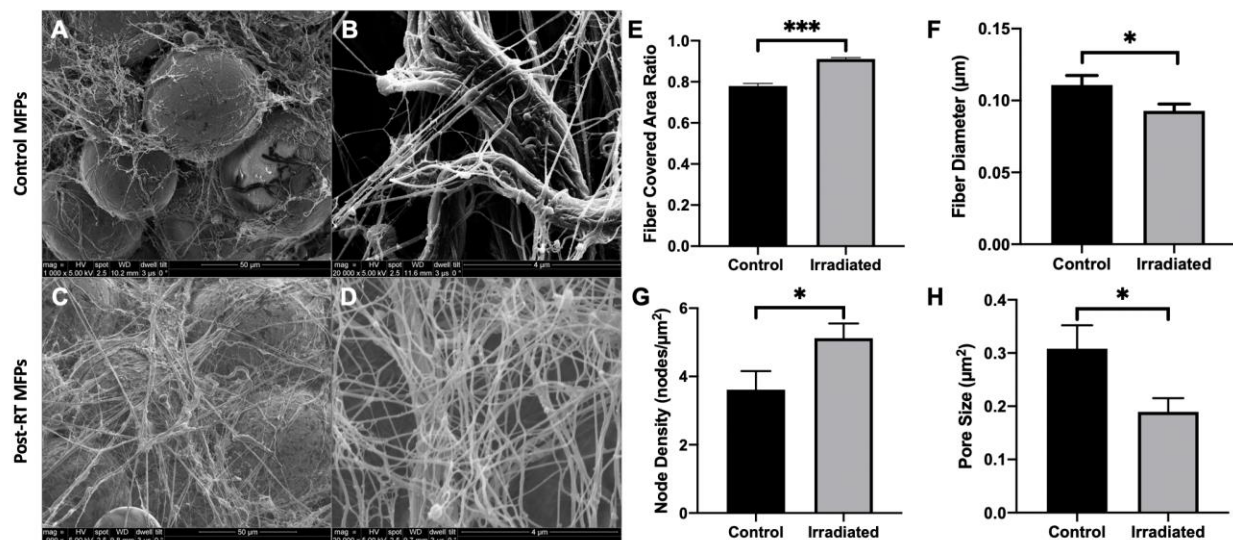| Raman Shift (cm^{-1})	Assignment	Control	Irradiated
1440	Protein/Lipid	1	1
1330	Lipid	0.475	0.453
1265	Amide III (collagen)	0.409	0.516
1660	Amide I (collagen)	0.537	0.731
1070	DNA	0.385	0.383
927	C-C stretching	0.204	0.316
1126	Lipid/Protein/Proteoglycan	0.282	0.368

Figures

Figure 1. Structure of control and post-RT MFPs by SEM and fiber network analysis. SEM images of unirradiated control MFPs from Nu/Nu mice (n = 10) at 1,000x (**A**) and 20,000x (**B**) magnification. SEM images of *ex vivo* irradiated (20 Gy) MFPs from Nu/Nu mice (n = 10) at 1,000x (**C**) and 20,000x (**D**) magnification. SEM images were analyzed using an automated fiber tracking algorithm to determine the fiber covered area ratio (**E**), average fiber diameter (**F**), node density (**G**), and pore size (**H**). Statistical significance was determined by ANOVA analysis with *p<0.05 and ***p<0.001. Error bars show the 95% confidence limit.
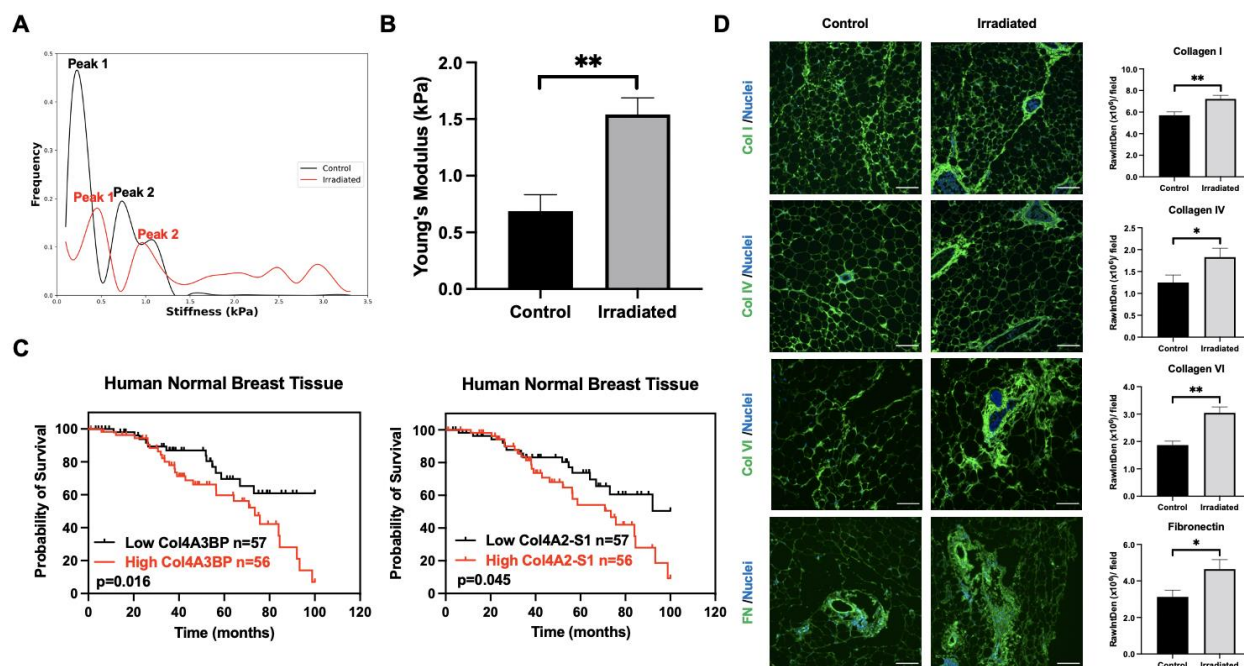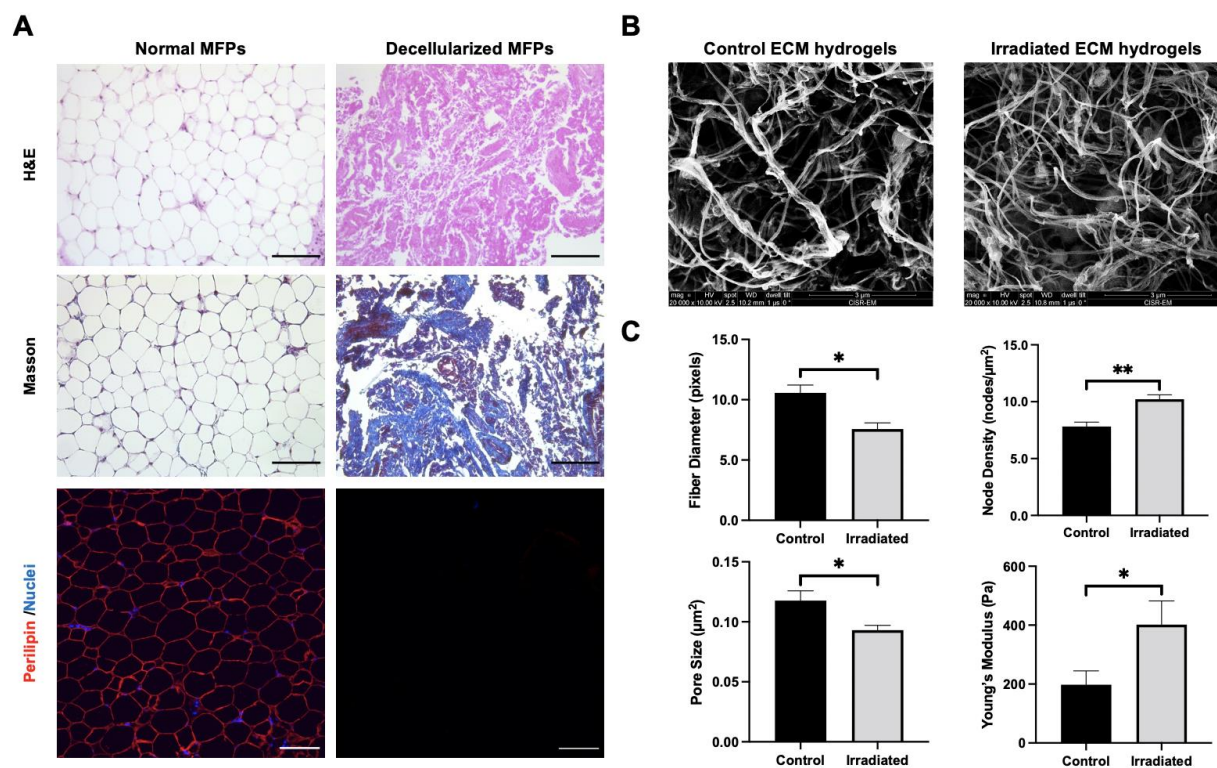
Figure 2. MFP irradiation enhances tissue stiffness and ECM deposition. (**A**) Stiffness distribution of control and *ex vivo* irradiated (20 Gy) MFPs from Nu/Nu mice (n = 4). (**B**) AFM analysis of the Young's moduli of control and *ex vivo* irradiated MFPs using the Hertz model. (**C**) Kaplan-Meier curves of human normal breast tissue patients with low versus high mRNA expression of *Col4A3BP* and *Col4A2-S1* (n = 113 patients) from GTEx normal breast tissue analysis. Immunofluorescence (IF) was performed to detect collagen I, collagen IV, collagen VI, and fibronectin in MFPs, and the corresponding quantification of fluorescence intensity is shown in (**D**). Scale bars are 100 μm. Statistical significance was determined by ANOVA analysis with *p<0.05 and **p<0.01. Error bars show the 95% confidence limit.
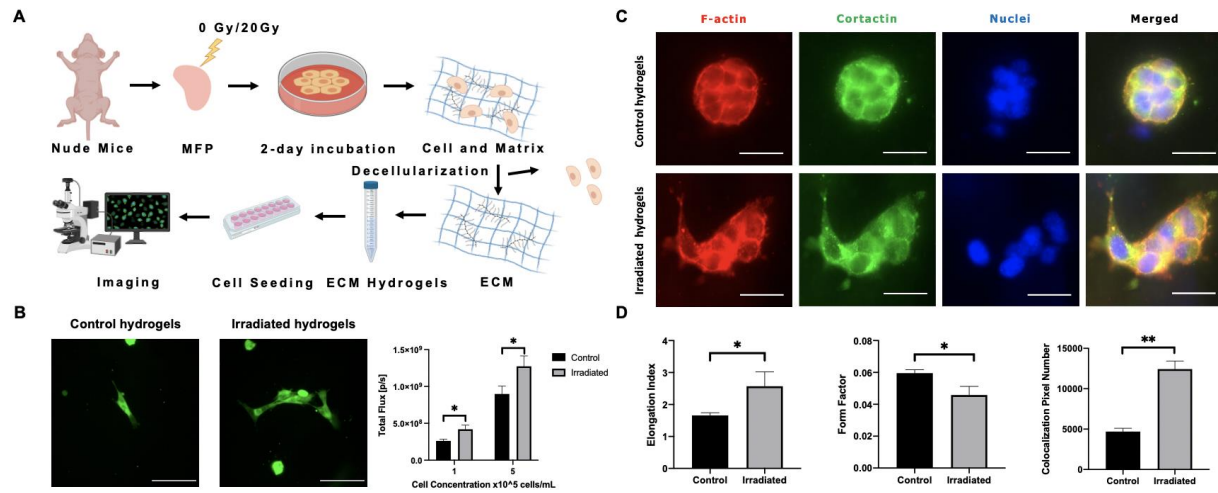
Figure 3. Characterization of decellularized ECM hydrogels from Nu/Nu mice. (**A**) H&E, Masson's Trichrome and perilipin staining of pre- and post-decellularized control MFPs confirmed decellularization and delipidation. Scale bars are 100 μm. SEM images of control and irradiated ECM hydrogels at 20,000x magnification (**B**), and the average fiber diameter, node density, pore size and mechanical properties (determined by AFM) were evaluated (**C**). Statistical significance was determined by ANOVA analysis with **p<0.01 and *p<0.05. Error bars show the 95% confidence limit.

Figure 4. 4T1 cell proliferation and invasion are enhanced in irradiated ECM hydrogels. (**A**) Schematic of experimental flow. (**B**) Fluorescence images of luciferase- and GFP-labeled 4T1 cells in ECM hydrogels from Nu/Nu mice (n = 3 for each condition) and bioluminescence quantification. (**C**) IF staining of F-actin, cortactin, nuclei and merged images for 4T1 cells embedded in control and *ex vivo* irradiated ECM hydrogels after 2 days. Scale bars are 100 μm. (**D**) Elongation index and form factor based on F-actin staining and colocalization pixel number as determined by cortactin-F-actin overlap were analyzed. Statistical significance was determined by ANOVA analysis with* p<0.05 and **p<0.01. Error bars show the 95% confidence limit.
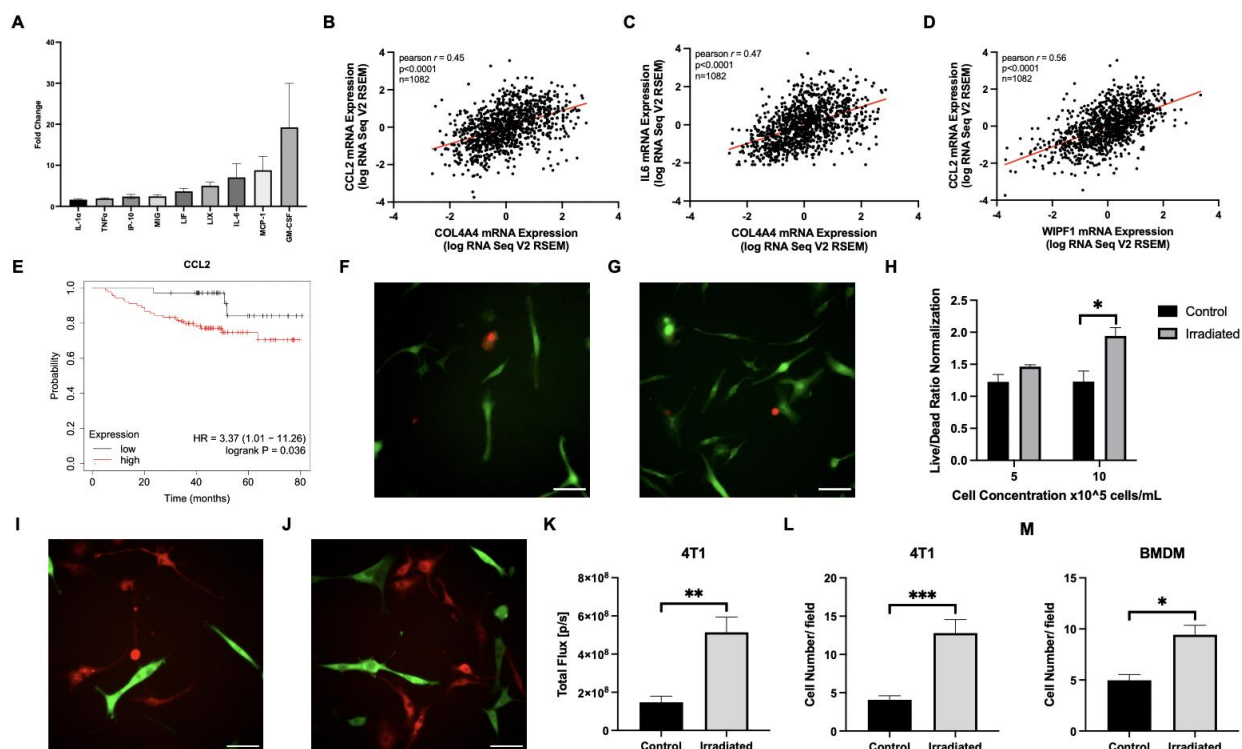
Figure 5. Irradiated microenvironments promote worse outcomes in patients and enhance tumor cell proliferation and tumor-macrophage interactions. (**A**) A Luminex assay was performed to determine the secreted cytokine profile of condition media from 4T1 cells cultured in the irradiated ECM hydrogels (n = 3). Data presented is mean fluorescence intensity (MFI) fold change compared to cytokine secretion from 4T1 cells cultured in the control ECM hydrogels. Only factors with a 1.5-fold or greater increase in MFI are shown. Correlation of *Col4A4* and *CCL2* mRNA expression (**B**), *Col4A4* and *IL6* mRNA expression (**C**), and *WIPF1* and *IL6* mRNA expression (**D**) from TCGA analysis (PanCancer dataset) in 1,082 patients with breast tumors. Pearson correlation shown. (**E**) Kaplan-Meier curves of TNBC patients with low versus high mRNA expression of *CCL2* from KMplotter. Fluorescence images of live (green) and dead (red) BMDM in control (**F**) and *ex vivo* irradiated (**G**) ECM hydrogels. (**H**) The normalized fluorescence intensity ratio of live to dead cells encapsulated in ECM hydrogels was quantified. Fluorescence images of co-cultures of luciferase-and GFP-labeled 4T1s and BMDM stained with CellTrace Far Red in control (**I**) and irradiated (**J**) ECM hydrogels with the corresponding bioluminescence quantification (**K**). Cell number per field of 4T1 (**L**) and BMDM (**M**) were quantified. Scale bars are 50 μm. Statistical significance was determined by ANOVA analysis with *$p<0.05$, **$p<0.01$ and ***$p<0.01$. Error bars show the 95% confidence limit.